Check for updates

Raditya Yudha Wiranegara
Centre for Propulsion and Thermal Power Engineering,
Cranfield University,
Cranfield, Bedfordshire MK43 0AL, UK
e-mail: raditya.wiranegara@outlook.com

Uyioghosa Igie[1]
Centre for Propulsion and Thermal Power Engineering,
Cranfield University,
Cranfield, Bedfordshire MK43 0AL, UK
e-mail: u.igie@cranfield.ac.uk

Pierre Ghali
Centre for Propulsion and Thermal Power Engineering,
Cranfield University,
Cranfield, Bedfordshire MK43 0AL, UK
e-mail: pierre.ghali@alten.co.uk

Rang Zhao
Centre for Propulsion and Thermal Power Engineering,
Cranfield University,
Cranfield, Bedfordshire MK43 0AL, UK
e-mail: rang.zhao@cranfield.ac.uk

David Abbott
Centre for Propulsion and Thermal Power Engineering,
Cranfield University,
Cranfield, Bedfordshire MK43 0AL, UK
e-mail: d.abbott@cranfield.ac.uk

Richard Hamilton
Mitsubishi Power Ltd.,
The Point, 37 North Wharf Road,
London W2 1AF, UK
e-mail: richard.hamilton.vp@mhi.com

Numerical Study of Radiation and Fuel–Air Unmixedness on the Performance of a Dry Low NOx Combustor

The development of gas turbine combustors is expected to consider the effects of radiation heat transfer in modeling. However, this is not always the case in many studies that neglect this for adiabatic conditions. The effect of radiation is substantiated here, concerning the impact on the performance, mainly the emissions. Also, the fuel–air unmixedness (mixing quality) influenced by the combustor design and operational settings has been investigated with regard to the emissions. The work was conducted with a Mitsubishi-type dry low NOx combustor developed and validated against experimental data. This 3D computational fluid dynamics study was implemented using Reynolds-averaged Navier Stokes simulation and the radiative transfer equation model. It shows that NO, CO, and combustor outlet temperature reduce when the radiative effect is considered. The reductions are 17.6% and below 1% for the others, respectively. Thus, indicating a significant effect on NO. For unmixedness across the combustor in a non-reacting simulation, the mixing quality shows a direct relationship with the turbulence kinetic energy (TKE) in the reacting case. The most significant improvements in unmixedness are shown around the main burner. Also, the baseload shows better mixing, higher TKE, and lower emissions (particularly NO) at the combustor outlet, compared to part-load. [DOI: 10.1115/1.4055983]

Keywords: combustion, computational fluid dynamics

1 Introduction

Stringent measures on capping stationary gas turbine emissions have been driving its combustor development towards lean-premixed combustion (LPC). Lean mixture enables gas turbine combustors to operate with relatively lower peak flame temperature compared to the peak temperature in a diffusion-type combustor, resulting in lower NOx emissions for the former. Fuel-rich pockets within the fuel–air mixture, which are known for inducing local hot-spots and eventually regions of high thermal NOx, are eradicated by establishing the mixing prior to the combustion primary zone. Therefore, these prominent features of the LPC have placed it at the forefront of the low NOx emissions combustion method [1–5].

Flame radiation has been long established to be a major contributor to the total heat flux to combustor liner walls in gas turbines and most industrial burners [6–9]. In the LPC case, the flame radiation is less observed than in the non-premixed combustion. This is due to its relatively small radiative heat loss, which is mostly the case at atmospheric pressure. However, the NOx formation kinetics sensitivity to high temperatures and the possibility of utilizing the radiation signals (as a control strategy to tend to its flame instability) have both advanced the research in this field [10]. Despite its importance, radiation was often neglected in computational fluid dynamics (CFD) studies due to its numerous numerical approach, computational costs, and uncertainty in the optical properties of elements involved [11]. Nevertheless, increasing computational capabilities and advancement of combustion and flame modeling paves the way for radiative heat transfer to be modeled in recent studies [12]. At least two radiative heat transfer models are found in combustion numerical studies; these are the P1 and discrete ordinates (DOs). Comparative studies by Ebrahimi Fordoei and Mazaheri [13] and Khodabandeh et al. [14] are in favor of DO rather than P1. The DO has shown a more accurate prediction of the experimental data compared to the other. Their results show that P1 predicts more radiation losses. Pang et al. [15] performed similar comparisons accounting for the same set of radiation models. The study was further carried out with P1, instead of DO, due to the latter computational demand from solving a finite number of discrete solid angles. The P1 is shown to have the best trade-off between accuracy and computational cost.

The concept of fuel–air unmixedness was first developed by Danckwerts [16]. He used the term intensity of segregation, I, to describe the "goodness of mixing" of a mixture between two components. If the value of I is 0, the mixture is perfectly mixed. On the other end, the value of 1 means complete segregation, i.e., the species are stirred yet unmixed [1,17]. In mathematical terms, an

[1]Corresponding author.

Manuscript received February 20, 2022; final manuscript received October 6, 2022; published online November 11, 2022. Assoc. Editor: Ioannis K. Nikolos.

Copyright © 2022 by ASME; reuse license CC-BY 4.0

Downloaded from http://asmedigitalcollection.asme.org/openengineering/article-pdf/doi/10.1115/1.4055983/6942616/aoje_1_011051.pdf by guest on 22 November 2022

I of a fuel can be defined as a ratio between the variance of fuel and the mean fuel concentration within the mixture. Hornsby and Norster [18] developed another formulation parameterizing the fuel–air unmixedness using fuel distribution mass-weighted average standard deviation at the investigated plane. Unlike the previous formulation, it does not recognize the value 1 to characterize the unmixed quality. Instead, it can be of any value above 0, as a function of mass-based fuel–air ratio (FAR). Li et al. [5] approached the fuel–air unmixedness by taking the ratio between the root mean square of the mixture fraction and the mass-weighted average of the mixture fraction. This ratio value is also bounded between 0 and 1, with a similar interpretation as in the first formulation. Other studies have investigated the unmixedness in relation to combustion emissions, particularly NOx. In a two-step experiment by Fric [1], fuel–air unmixedness of a combustor model was measured in non-reacting (cold) flow using NO_2 laser-induced fluorescence, followed by NOx emissions measurement in reacting flow. Both steps were performed at atmospheric pressure and concluded that it is insufficient to consider only spatial unmixedness when assessing the premixer effectiveness in reducing NOx emissions. It was shown that NOx emission is highly sensitive to even a small level of temporal unmixedness. The effect of different operating pressures ranging from 1 to 30 bar and fuel–air unmixedness on NOx emissions was investigated by Biagioli and Güthe [19]. Experimental and numerical works were carried out on an industrial gas turbine combustor. The work looked at how the unmixedness and operating pressure affect the formation of NOx from two pathways, i.e., the fast-forming NO prompt and the slow-forming one, post flame (or, in general term, thermal). It was concluded that NOx emissions become gradually more sensitive to unmixedness as the pressure increases. Hence, the increase of NOx emissions due to the unmixedness at atmospheric pressure is lower than at 30 bar operations. Li et al. [5] also performed an experimental and numerical study of fuel–air unmixedness. This involved using a low-aspect-ratio dump combustor running on methane. Two values of turbulent Schmidt number, i.e., 0.5 and 0.9, were tested in the numerical work, which shows significant effects on the fuel–air unmixedness. The study highlights similar outcomes with previous works, emphasizing the challenge of using Reynolds-averaged Navier Stokes-CFD with constant turbulent Schmidt number.

In this study, dry low NOx (DLN) combustor inspired by Mitsubishi-type technology has been developed. This has been complemented with public domain information from Refs. [20,21]. The model consists of key features of Mitsubishi-type technology and is supported with a study on the validation of the computational methodology with the experimental work of Ruan et al. [22]; an approach also used by Emami et al. [23]. This is due to a lack of experimental data on the exact combustor deployed. This work shows:

- The use of the P1 radiation model to calculate the radiative heat transfer from the combustion flame to its adjacent environment at baseload operation of a gas turbine.
- The relationship between fuel–air unmixedness and combustion flow fields at the baseload and part-load operations, alongside the emissions.

2 Methodology

2.1 Turbulence Modeling. The two-equation eddy-viscosity-based model: the k–ε model that widely used combustion flow analysis was considered. One of the variants of the standard k–ε model (SKE) known as the realizable k–ε model (RKE) was chosen for this study to address the drawback of the SKE. This has to do with the fact that SKE tends to be over-diffusive in predicting highly swirling flow. Hence, it can significantly affect predictions of the fuel–air mixing process that relies on swirled flow. As such, the RKE has been the most favored model in reacting flow simulation [24–28]. The term "realizable" indicates the model capability in meeting certain mathematical constraints imposed by the Reynolds stresses, therefore, consistent with the physics of the turbulent flow.

In addition to turbulence modeling, a non-reacting and reacting flow simulation have been considered. Each case helps to establish the relationship between fuel–air unmixedness, and combustion performance and emissions. The non-reacting flow simulation provides a way to evaluate the aerodynamic behavior of fuel–air mixing independent of combustion effects. These factors play a crucial role in combustion reaction that impacts performance and emissions. The non-reacting simulation was carried out by solving each chemical species transport equation in Eq. (1), for the fuel (pure methane—CH_4) and oxidizer (air—O_2 and N_2). The equation was solved without the modeling of the reaction source term, $\overline{\omega_k}$, therefore no reaction between the fuel and oxidizer is taking place for the non-reacting flow. As shown from the equation, the output is a scalar variable of the local mass fraction of each species, Y_k. From here, the quality of mixing can then be determined, in this work.

$$\frac{\partial \widetilde{Y}_k \bar{\rho}}{\partial t} + \frac{\partial}{\partial x_i}(\widetilde{Y}_k \bar{\rho} \widetilde{u_j}) = \frac{\partial}{\partial x_i}(-\bar{\rho}\widetilde{V_k Y_k}) + \overline{\omega_k} - \frac{\partial}{\partial x_i}(\bar{\rho}\widetilde{u_i' Y_k'}) \tag{1}$$

2.2 Combustion Model—Flamelet Generated Manifold. The combustion flame model used is the flamelet generated manifold (FGM) to account for operations in which the flame operates in a mix between diffusion and premixing. It is a hybrid model notably known as a partial-premixed combustion model. The FGM shares a similar assumption with the flamelet theory [29] that a multi-dimensional turbulent flame consists of an ensemble of one-dimensional laminar flames. All thermochemical scalars are embedded within each flame from which a manifold is constructed and retrieved during the simulation. The manifold or database is parameterized by two controlling scalar variables, namely, the mixture fraction (f) and reaction progress (c). The use of the reaction progress in the framework is to mitigate a flaw from the mixture fraction, as it does not have inherent information on the progress of involving chemical reactions [30]. These variables are typically presented in the form of density-weighted average variables with the respecting transport equations written as

$\tilde{f}$ − equation:

$$\frac{\partial \rho \tilde{f}}{\partial t} + \frac{\partial}{\partial x_i}(\tilde{f}\widetilde{u_j}\rho) = \frac{\partial}{\partial x_j}\left[\left(\frac{k}{C_p} + \frac{\mu_t}{\sigma_k}\right)\frac{\partial \tilde{f}}{\partial x_j}\right] \tag{2}$$

$\tilde{c}$ − equation:

$$\frac{\partial \rho \tilde{c}}{\partial t} + \frac{\partial}{\partial x_i}(\tilde{c}\widetilde{u_j}\rho) = \frac{\partial}{\partial x_j}\left[\left(\frac{k}{C_p} + \frac{\mu_t}{\mathrm{Sc}_t}\right)\frac{\partial \tilde{c}}{\partial x_j}\right] + \rho S_c \tag{3}$$

where C_p is the heat capacity at constant pressure, Sc_t is the Schmidt number for turbulent flow, and S_c is the source term for the reaction progress.

In addition to these scalars, the FGM also solves another transport equation for mixture fraction and reaction progress variances, $\widetilde{f'^2}$ and $\widetilde{c'^2}$, to account for fluctuation of local mixture fraction caused by turbulence eddies. The scalar variables obtained from solving these transport equations are then embodied in the development of mean thermochemical properties of the mixture database, through the assumed joint probability density functions (PDFs) model, $P(c, f)$. This is calculated as

$$\tilde{Y} = \iint Y(c, f, \tilde{H}) P(c, f) dc df \tag{4}$$

where

$$\tilde{Y} = \tilde{Y}(\tilde{c}, \widetilde{c'^2}, \tilde{f}, \widetilde{f'^2}, \tilde{H}) \tag{5}$$

The PDF of each control variable in the joint PDFs model, $P(c, f)$, can be calculated independently. Hence,

$$P(c, f) = P(c)P(f) \tag{6}$$

Downloaded from http://asmedigitalcollection.asme.org/openengineering/article-pdf/doi/10.1115/1.4055983/6942616/aoje_1_011051.pdf by guest on 22 November 2022

In this work, the shape of the joint PDF model, $P(c, f)$, is described using the assumed β-function. While the above equations only show the species mass fraction, Y, the implementation applies to other thermochemical properties, such as temperature, density, and specific heat.

In the model, non-adiabatic application, an additional energy-related scalar, is included in the integration of the right hand side (RHS) terms. The scalar is enthalpy, H, represented in its density-weighted average value and obtained from solving its transport equation. The equation includes S_H, a source term to account for radiation and other forms of heat transfer with wall boundaries.

The modeling of a partially premixed combustion framework also requires a model to close the reaction progress source term, S_c, in Eq. (2). An equation replaces the term with

$$\rho S_c = \rho_u U_t |\nabla \tilde{c}| \tag{7}$$

where ρ_u is the unburnt mixture density and U_t is the turbulent flame speed. A model for wrinkled and thickened flame front has been developed by Zimont [31] to define the turbulent flame speed. The model describes the varying influences of turbulence eddy scales on laminar flamelet [31]. The small-scale eddies thicken the flamelet and intensify its propagation velocity. The large ones, subsequently, wrinkle the thickened flamelet and control the expansion of the combustion zone. Based on the description, there are at least two key considerations that the model must cover, namely, the laminar flame speed, U_l, and the flame front shape-changes by the turbulence eddies. Mathematically, this is

$$U_t = A u'^{3/4} U_l^{1/2} \chi_u^{-1/4} l_t^{1/4} \tag{8}$$

where A is a prefactor with a value of 0.52, which is obtained experimentally and shows good accuracy across a range of different fuels and operating conditions [31], u' is the instantaneous (root mean square) velocity, χ_u is the molecular heat transfer coefficient of the unburnt mixture, and l_t is the turbulent length scale. The laminar flame speed and unburnt molecular heat transfer coefficient can be obtained from experiments or one-dimensional laminar flame simulation with a detailed chemical mechanism. The latter was selected for the work here.

To predict NO_X, a separate transport equation for NO mass fraction, Y_{NO}, is used, as expressed in Eq. (9). This modeling based on NO was obtained as post-processing step, after the convergence of the combustion simulation. It is important to indicate that this approach is considered because the FGM assumption of rapid chemistry may not be suitable for the prediction of NOx emissions [22,32,33]. This is because NOx formation, which takes several pathways, has a generally longer chemical time scale than the turbulent time scale, consequently resulting in the ratio of these scales, known as Damköhler number, always being below unity.

$$\frac{\partial \rho \widetilde{Y_{NO}}}{\partial t} + \frac{\partial}{\partial x_i}(\widetilde{Y_{NO}} \tilde{u}_j \rho) = \frac{\partial}{\partial x_j}\left[\rho D \frac{\partial \widetilde{Y_{NO}}}{\partial x_j}\right] + S_{NO} \tag{9}$$

where $\widetilde{Y_{NO}}$ is the mass fractions of NO, and D is the effective diffusion coefficient. The NO reaction source term, S_{NO}, is defined differently depending on the chosen NO formation pathway. Three pathways are considered in this work, namely, thermal, prompt, and intermediate N_2O mechanisms. An extended Zeldovich mechanism is employed to describe the thermal NO formation. The prompt NO formation is described by the De Soete model [34]. Finally, an additional transport equation is solved to obtain the N_2O mass fraction, by which its influence is described by the formation mechanism proposed in Ref. [35].

Turbulence plays a vital role in combustion. The temporal fluctuations in temperature and species concentrations, resulting from the turbulent mixing process, affect the flame characteristics, hence the NO formation rates. The relationships between these variables are highly non-linear, and their fluctuations have to be taken into consideration. One way of doing so is via a PDF. The PDF is assumed using β-function, similar to the one used in the FGM modeling.

The mean NO reaction source term is defined through the following equation:

$$\overline{S_{NO}} = \int_0^{V_{max}} M_{w,NO}\left(\frac{d[NO]}{dt}\right)_{total} P(v)dv \tag{10}$$

where $M_{w,NO}$ is the molecular weight of NO, v is a fluctuation variable, and $P(v)$ is the PDF of variable v. The total NO reaction rate, $(d[NO]/dt)_{total}$, is the sum of all NO reaction rates from the three NO formation pathways that are previously discussed. The upper limit for the integration of Eq. (10) is set to the variable's maximum value within the flow field.

2.3 Thermal Radiation Model. Thermal exchange through radiation is accounted for using the radiative transfer equation (RTE) that quantifies the rate of radiation intensity change along a path inside a medium. It describes the interaction on a macroscopic level, between radiation and matter with consideration of its ability to absorb, emit, and scatter radiant energy. Despite having similar conservation, RTE structure differs from the governing equations of the turbulent combustion flow. It is an integro-differential equation that depends on six variables. Three are spatial variables, two are direction variables, and one is a spectral (frequency range) variable [36,37]. The complexity of RTE mandates additional numerical approaches because analytically solving it is considered impractical for most engineering applications. Each approach has been tailored according to the RTE's variables dependency in space, direction, and spectral. In this work, the space and directional variables were solved using the P1 radiation model [38]. For the spectral variable, the weighted sum of gray gases model (WSGGM) was employed.

The P1 model [38] is the lowest order model within the spherical harmonics (usually denoted by P-N) family. In this model, the spatial and directional dependencies are decoupled through the expansion of the radiation intensity into a series of spherical harmonics. The series itself is expressed in a two-dimensional Fourier series, and truncating its first element gives the P1 model [36,39]. The model consists of two spatial differential equations, namely, the radiative heat flux, $q_{r,\eta}$, and its gradient, $\nabla q_{r,\eta}$, written in the following forms in Eqs. (11) and (12):

$$q_{r,\eta} = -\frac{1}{3(\kappa_\eta + \sigma_{s\eta})}\nabla G_\eta \tag{11}$$

$$\nabla q_{r,\eta} = 4\pi\kappa_\eta I_{b\eta} - \kappa_\eta G_\eta \tag{12}$$

where G_η is the spectral incident radiation. Equation (12) can be substituted into the energy equation to account for radiation effect on the combustion flow field. Through the integration of radiative intensity on the wall boundary and the application of the Marshak boundary condition [40], the wall radiative heat flux, $q_{r,w}$, can be expressed as follows in Eq. (13):

$$q_{r,w} = -\frac{\varepsilon_w}{2(2-\varepsilon_w)}(4n_{med}^2\sigma T_w^4 - G_w) \tag{13}$$

where ε_w is the wall emissivity, n_{med} is the refractive index of the medium, σ is the Stefan–Boltzmann constant, T_w is the wall temperature, and G_w is the incident radiation at the wall.

Before solving the spatial and direction dependencies, a spectral integration is initially performed to reduce the evaluation matrix's size. Also reducing the computational power to solve the RTE. A spectral WSGGM developed by Hottel and Sarofim [41] was considered in this work. Modest [42] extended its applicability to be used alongside the P1 model. It carries a basic assumption that the absorption coefficient is independent of the wavelength

Downloaded from http://asmedigitalcollection.asme.org/openengineering/article-pdf/doi/10.1115/1.4055983/6942616/aoje_1_011051.pdf by guest on 22 November 2022

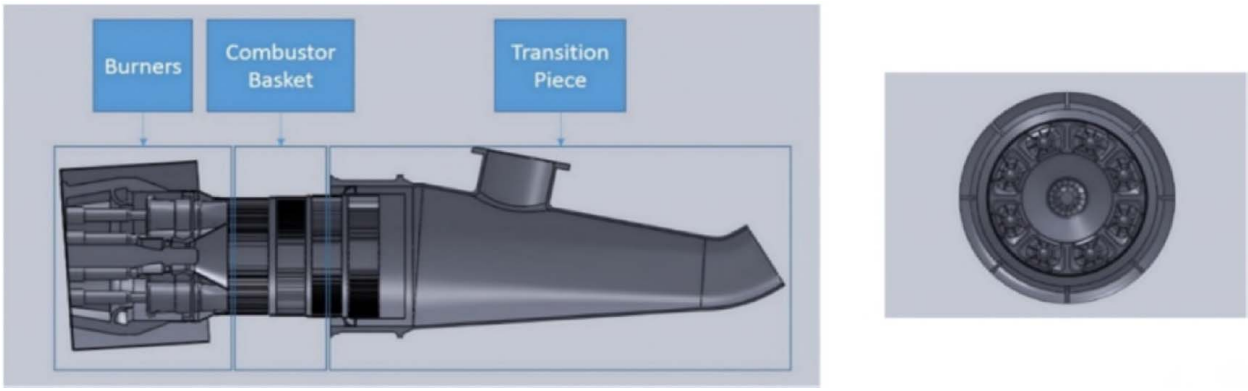


Fig. 1 3D combustor model

region, enabling the spectrum to be subdivided into several regions. This underlies the concept of the gray gas model, hence the name of the model. Thus, the absorption coefficient, κ, can be obtained from

$$\kappa = -\frac{\ln(1-\varepsilon)}{s} \tag{14}$$

In which

$$\varepsilon = \sum_{i=0}^{I} a_{\varepsilon,i}(T)(1 - e^{-\kappa_i \varrho s}) \tag{15}$$

$$s = 3.6\frac{\nu}{A} \tag{16}$$

where $a_{\varepsilon,i}$ is the emissivity weighting factor for the ith fictitious gray gas as a function of temperature, κ_i is the absorption coefficient of the ith fictitious gray gas, ϱ is the sum of partial pressures of all absorbing gases, ν is the volume of fluid and A is the total surface area of the fluid boundaries, e.g., inlets, outlets, and walls.

2.4 Fuel–Air Unmixedness. This work used the formulation by Hornsby and Norster [18] as it is suitable to evaluate fuel–air unmixedness from a CFD simulation. Hence, the fuel–air unmixedness will be deduced from the evaluation of the fuel distribution mass-weighted average standard deviation, S_f, written as

$$S_f = \sqrt{\frac{\sum C_n^2 W_n}{\sum W_n} - \left(\frac{\sum C_n W_n}{\sum W_n}\right)^2} \tag{17}$$

where C_n is the mass fraction of fuel at cell n and W_n is the mass flow through cell n. To be consistent with the general convention in the fuel–air unmixedness, S_f needs to be normalized to have the value bounded between 0 and 1. In this case, the variable is normalized with a coefficient derived from mass-based FAR, S_{FAR}

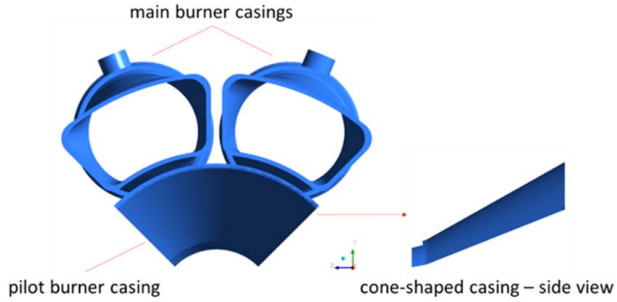


Fig. 2 Main burners casing, pilot burner, and side view of the cone-shaped pilot casing

[43]. Hence, the normalized variable is determined as

$$S_N = \frac{S_f}{S_{\text{FAR}}} \tag{18}$$

where

$$S_{\text{FAR}} = \sqrt{\left(\frac{\text{FAR}}{1+\text{FAR}}\right) - \left(\frac{\text{FAR}}{1+\text{FAR}}\right)^2} \tag{19}$$

3 Combustor Model

The combustor model developed is inspired by that found in Mitsubishi-type heavy-duty engine. Developing the combustor model began with some known dimensions of the combustor inner diameter and other estimates from Ref. [44]. Other dimensions were scaled from Refs. [20,45]. For details that could not be generated from public domain drawings (e.g., the thickness and angle of main and pilot swirl vanes), typical ranges of design variables from standard references such as Ref. [46] were employed. The combustor model has main burners, a pilot burner, a basket, and a transition piece shown in Fig. 1. The main burners are arranged circumferentially around the pilot burner. This is illustrated by the arrangement of the casings displayed in Fig. 2. Each of the burners consists of a fuel nozzle and swirler vanes surrounded by a tube. A cone-shaped part is attached to the outlet end of the pilot burner tube that is generally referred to as a flame holder. Cooling slots are added to the basket and the transition piece to maintain acceptable wall temperatures. In practice, this transition piece is connected to bypass from which diverts airflow from the combustor inlet. The effect of additional air with a lower temperature into the transition piece brings about a drop in the combustor outlet temperature. The amount of air into the bypass has a relationship with the engine load. For modeling, the engine manufacturer bypass scheduling in Ref. [47] has been implemented. The burners produce different types of flame; the mains produce premixed flame while the pilot produces diffusion flame. To reduce emissions, both burners operate with lean fuel–air mixtures at the design or baseload operation. The diffusion flame that is known for wide stability limits ensures stable combustion, being anchored close to the pilot burner outlet using the flame holder. The flame holder aerodynamically induces a recirculating zone downstream which feeds the flame with a continuous supply of the pilot fuel–air mixture. The heat release from this zone, referred to as the central recirculation zone, radiates toward the main fuel–air mixture to produce a set of premixed flames, therefore increasing the primary zone combustion temperature, further.

The model features an axis of symmetry that can typically benefit from periodicity in simulation. However, the flow in a section of the model can effectively be cut around the axis of symmetry, still yielding a complete representative solution. Hence a quarter section of the combustor shown in Fig. 3 was used in this work.

Downloaded from http://asmedigitalcollection.asme.org/openengineering/article-pdf/doi/10.1115/1.4055983/6942616/aoje_1_011051.pdf by guest on 22 November 2022

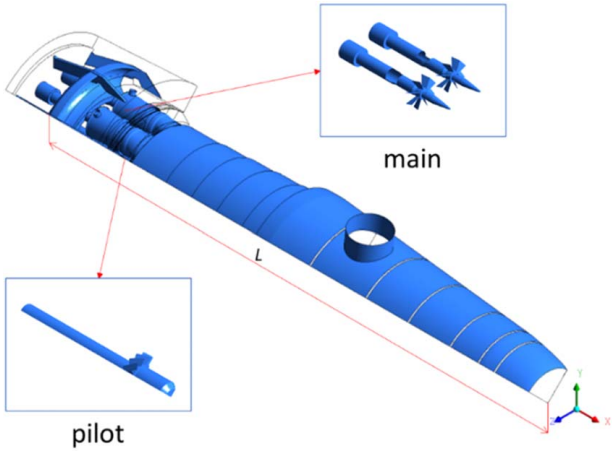


Fig. 3 The quarter section model of the combustor

This significantly reduced the computational effort without compromise to accuracy.

3.1 Mesh and Independence Study. The computational mesh was generated using ICEM-CFD. Due to the complexity of the burner geometry, the domain was discretized using both tetrahedral and hexahedral meshes. As shown in Fig. 4, the tetrahedral mesh was generated for the burners and a part of the transition piece (where the bypass valve attaches). The hexahedral mesh was generated for the chamber and the rest of the transition piece. Three meshes of different resolutions (6.3, 10.6, and 23.1 million) in nodes were generated. The use of the RKE model mandates a y^+ above 30 in the inner layer of the log-law region since it employs a standard wall function to capture the near-wall physics, instead of having an increased resolution to resolve the flow directly. Therefore, to ensure that only the grid resolution affected the results, the boundary layer was kept uniform across these meshes. On the medium mesh, the calculated runtime for every 1000 iterations running on 64 CPU cores was approximately 0.5 and 1.7 times that of the fine and coarse meshes, respectively.

Except for reaction progress, the quantities of selected flow outputs have been normalized with their global reference values (defined as the maximum value in each plot). The normalized quantities were then plotted against the normalized axial position, (x/L), where L is the combustor length as in Fig. 3. From the mesh comparisons, the medium mesh was selected for providing the best compromise between computational time and consistency in accuracy as shown in Fig. 15 of Appendix A. Figure 5 shows more details of the internal parts with boundary conditions consisting of the combustor inlet, fuel inlets, cooling inlets at the midsection and transition piece, combustor outlet, and solid walls. The inset on the figure shows a magnified version of the burners, also a better view of the fuel and cooling inlets.

Pressure and temperature are defined at the combustor inlet. Mass flowrate and temperature are defined at the cooling inlets, with the temperature set the same as in the inlet. The flow parameters defined at the fuel inlets are mass flowrate and temperature. The fuel considered in this work is pure methane (CH_4). Backflow temperature and progress variable are defined at the outlet with the values reflecting the expected temperature of complete combustion in which $c = 1$. On the solid walls, a non-slip boundary is defined. Wall emissivity and temperature are additionally defined on the liner walls within the basket and transition piece. The material was assumed to be Nimonic, hence with the emissivity of 0.7 [47]. In the absence of experimental data, the wall temperature was assumed to be uniform with the value of 1000 K. The number is considered a reasonable estimate of the liner wall operating temperature, as it incorporates a cooling.

Baseload and part-load conditions were considered in this study. The corresponding engine-level performance and boundary conditions were obtained from Ref. [48] in the same TURBO-REFLEX project. The refereed work was conducted using Cranfield's in-house code, TURBOMATCH that simulates gas turbine engine performance with the provision of combustor inlet and outlet temperatures, pressures, and flows. The fuel split ratio between the main and pilot and its scheduling against load captured in the CFD model was based on the schedule in Ref. [21] and the engine manufacturer recommendation. Table 1 shows the boundary conditions used in the model, obtained from the engine model of Abudu et al. [48].

3.2 Verification of Combustion Behavior. Due to the lack of exact experimental data on the combustor model used, the model was simulated at similar conditions as Ref. [22] with similar computational methodology. The referred work was conducted at atmospheric pressure without the pilot, i.e., no fuel is injected through the pilot fuel inlets. Hence, the diffusion flame is not ignited. However, while having a similar burner configuration, Ruan et al. [22] does not include the film cooling slots and perforated holes at locations indicated in the reference model; as such, not also an exact comparison. Two axial plane locations from the inlet of the burner were considered. Figure 6 shows their radial profiles of temperature and CO_2 mass fraction. Small differences are observed between the current simulation and the reference experimental work. At plane A, the maximum percentage error for temperature is ~31% and for CO_2 is ~124%. At plane B that is 0.087 m from plane A, the errors are less, with ~3% and ~13%, respectively.

4 Influence of Radiation on Performance and Emissions

This part of the work examines the influence of radiation on the performance and emissions at the baseload. Implementing radiation in the simulation is expected to allow the heat flux from the combustion flame to be distributed to its surroundings. The comparison to the non-radiative case proves that the temperature in the combustion primary zone drops as a result. This brings about a drop in the NO and CO shown in Table 2. The NO formation pathways described previously were also considered in the comparisons. It should be noted that the absolute value of the emissions level has been previously corrected to 15% O_2. The positive change observed for the NO–N_2O pathway indicates a higher absolute value in the non-radiative case than in the radiative one. This is because of the promotion of the slow formation of the N_2O ($NH + NO \rightarrow N_2O + H$) as the result of the drop in temperature. As for the thermal and prompt NO, there is a decrease also for the same reason. The mechanism of these emissions requires a large amount of energy and the drop in temperature reduces the amount of energy required. Though

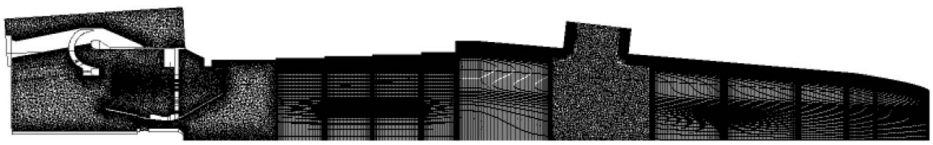


Fig. 4 Reduced model computational mesh

Downloaded from http://asmedigitalcollection.asme.org/openengineering/article-pdf/doi/10.1115/1.4055983/6942616/aoje_1_011051.pdf by guest on 22 November 2022

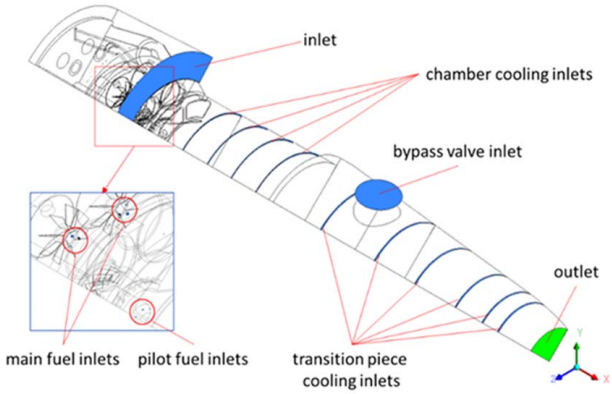


Fig. 5 Boundary conditions on the model

Table 1 Boundary conditions of baseload and part-load [48]

Parameters	Baseload	Part-load
Gas turbine load	100%	68%
Inlet air pressure	15.9 bar	12.2 bar
Inlet air temperature	692 K	654 K
Fuel	CH_4	CH_4
Inlet fuel temperature	413	413
Total air inlet mass flowrate	23.5 kg/s	18.4 kg/s
Bypass valve air inlet mass flowrate (% of total inlet)	0	8.72
Global FAR	0.0293	0.0275
Global equivalence ratio	0.53	0.50
Mains equivalence ratio	0.61	0.58
Pilot equivalence ratio	0.56	1.33

being lower than in the non-radiative simulation, the effect of the temperature on the CO is relatively minor. However, the overall reduction of NO is more significant and relates to the fact that the increase is an exponential function of temperature. The change in the NO is due to radiation that is approximately ~45 times that of the CO.

Figure 7 shows the axial profiles for both cases, indicating the normalized temperature profiles. This shows similar temperature trends from the starting point (burner outlet) to the endpoint 1, that is the outlet of the transition piece. There is a gradual increase in the temperature that peaks around $x/L = 0.65$. This is attributed to the ignition of the lean-premixed mixture produced by the premixed burners. The ignition itself is caused by the heat from the diffusion flame produced by the pilot burner that propagates downstream. This can be observed from the contour plot of temperature shown on the right of the figure. In both simulations, the combustor liner walls are treated as non-adiabatic and have a relatively lower temperature than the gas within the primary combustion zone. Hence, the reduction in the peak temperature for the radiative case is mainly due to the heat exchange between the hot combustion gas and its adjacent environment (including the liner wall incorporating the P1 radiation model). The inset shows that the non-radiative case

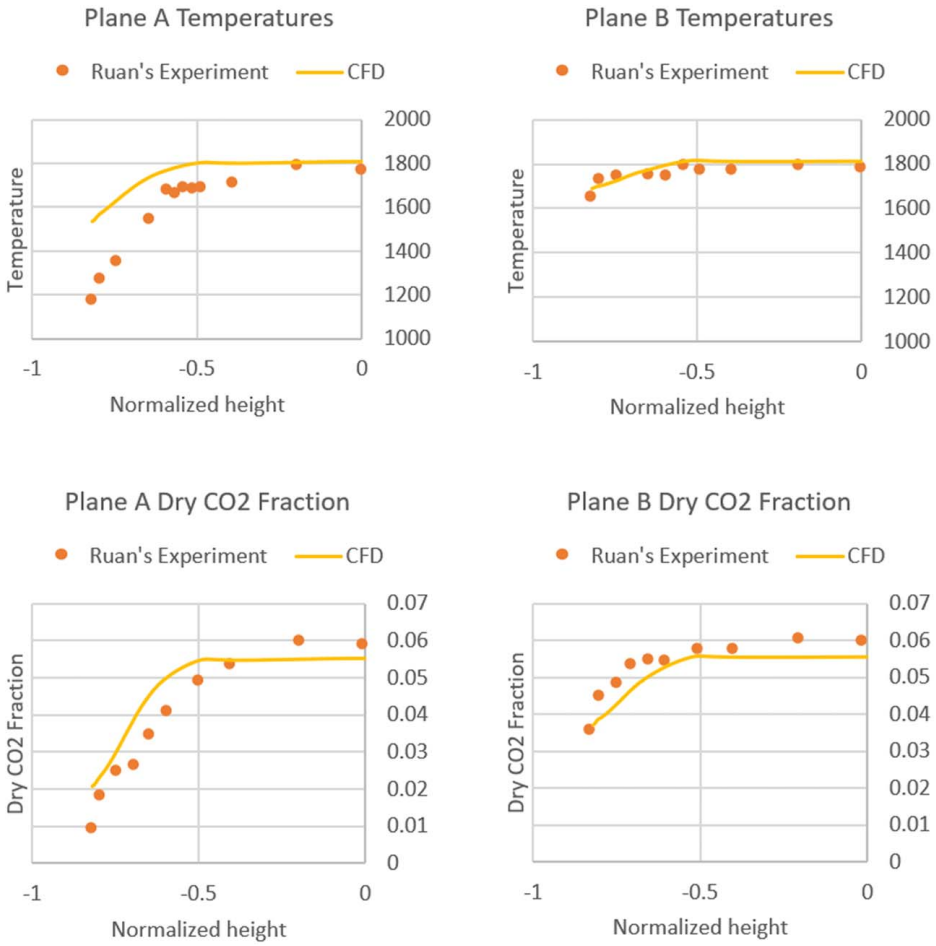


Fig. 6 Radial profiles of temperature (top) and mass fractions of CO_2 (bottom) at planes A and B

Downloaded from http://asmedigitalcollection.asme.org/openengineering/article-pdf/doi/10.1115/1.4055983/6942616/aoje_1_011051.pdf by guest on 22 November 2022

Table 2 Change in outlet temperature and emissions relative to the non-radiative case

		NO			
Temperature	CO	Total	Thermal	Prompt	Via N_2O
−0.41%	−0.97%	−17.63%	−24.80%	−20%	10%

has the higher values, repeated small reductions in temperature are seen in the profiles, starting from $x/L = 0.5$ up to $x/L = 1$. These reductions are due to the cooling air flowing through the cooling slots in the transition piece shown on the right of the figure.

The corresponding CO and NO axial profiles are shown in Fig. 8. The peak CO formation is observed between $x/L = 0.3$ and $x/L = 0.4$; also see inset 1 in the figure, with the non-radiative simulation being the lower of the two. The difference within the range is observed to be minor, ∼0.56%. The rate of CO burnout, from $x/L = 0.4$ onwards, is about the same, with the radiative simulation still showing to be slightly higher than the non-radiative. However, as shown from inset-2, after $x/L = 0.85$, the CO of the non-radiative simulation is slightly greater by a few percentages, ∼0.03%. This can be attributed to a better heating distribution in the radiative model. As a result, the CO burnout rate in the radiative case is slightly steeper than in the non-radiative case. The negligible difference indicates that the radiation model does not significantly affect the CO emission.

As for the NO axial profiles also shown in Fig. 8, the radiative case is shown to be always below the non-radiative one. The formation rate is at its highest below $x/L = 0.2$, which is consistent with the rapid increase of the combustion temperature induced by the diffusion flame produced by the pilot burner. Beyond this point, the NO concentration for both cases grows at a lower rate and plateaus towards the end of the combustor. This most significant difference between both cases is seen at the combustor outlet. The profile highlights the marked lower NO for the radiative case for a relatively small temperature change shown in Fig. 7. In terms of the formation pathway, the thermal pathway remains the dominant mechanism, contributing up to ∼73% of the total NO. It is about 7% less than the non-radiative case. The N_2O pathway contributes ∼28%, which is approximately 7% more than in the non-radiative case. As such, the inclusion of the radiation model is seen to provide a better representation of a gas turbine operating under a lean-premixed fuel–air mixture at a high-pressure condition. The prompt pathway makes a negligible contribution.

The radial profiles for the non-radiative and radiative cases are shown in Fig. 9. Each profile was extracted at normalized axial positions that describe key locations of the combustion processes. The normalized parameters are plotted for the normalized radial position (y/R), where R is the combustor radius at the normalized axial position. The figure shows that at each axial location, the temperature profiles of both cases follow each other closely, yet the radiative profiles remain below the non-radiative ones in all cases. The most significant difference is seen at axial location $x/L = 0.19$ situated closer to the burner outlet, where the flame temperature is at its highest. The high-temperature region extends around the combustor central part (from $y/R = 0$–0.5) before a significant drop towards the liner wall where $y/R = 1$. The central part region is mainly influenced by the diffusion flame produced by the pilot burner with a

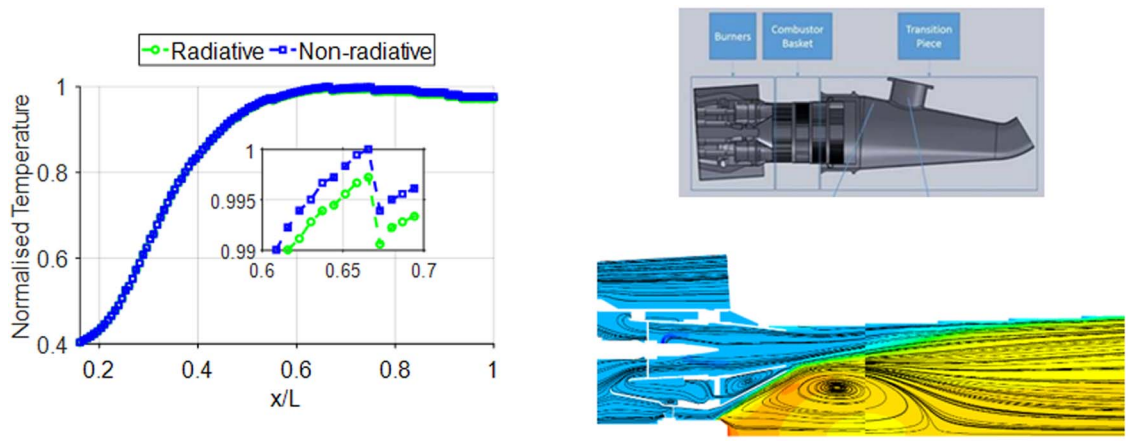


Fig. 7 Axially averaged temperature across the combustor (left) 3D model and contour of the temperature (right)

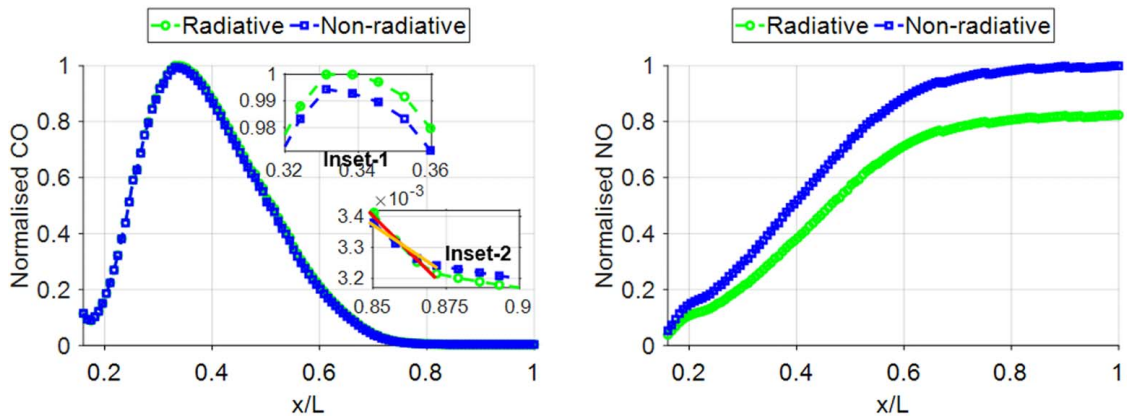


Fig. 8 Axial mass-averaged CO and NO for radiative and non-radiative cases

Downloaded from http://asmedigitalcollection.asme.org/openengineering/article-pdf/doi/10.1115/1.4055983/6942616/aoje_1_011051.pdf by guest on 22 November 2022

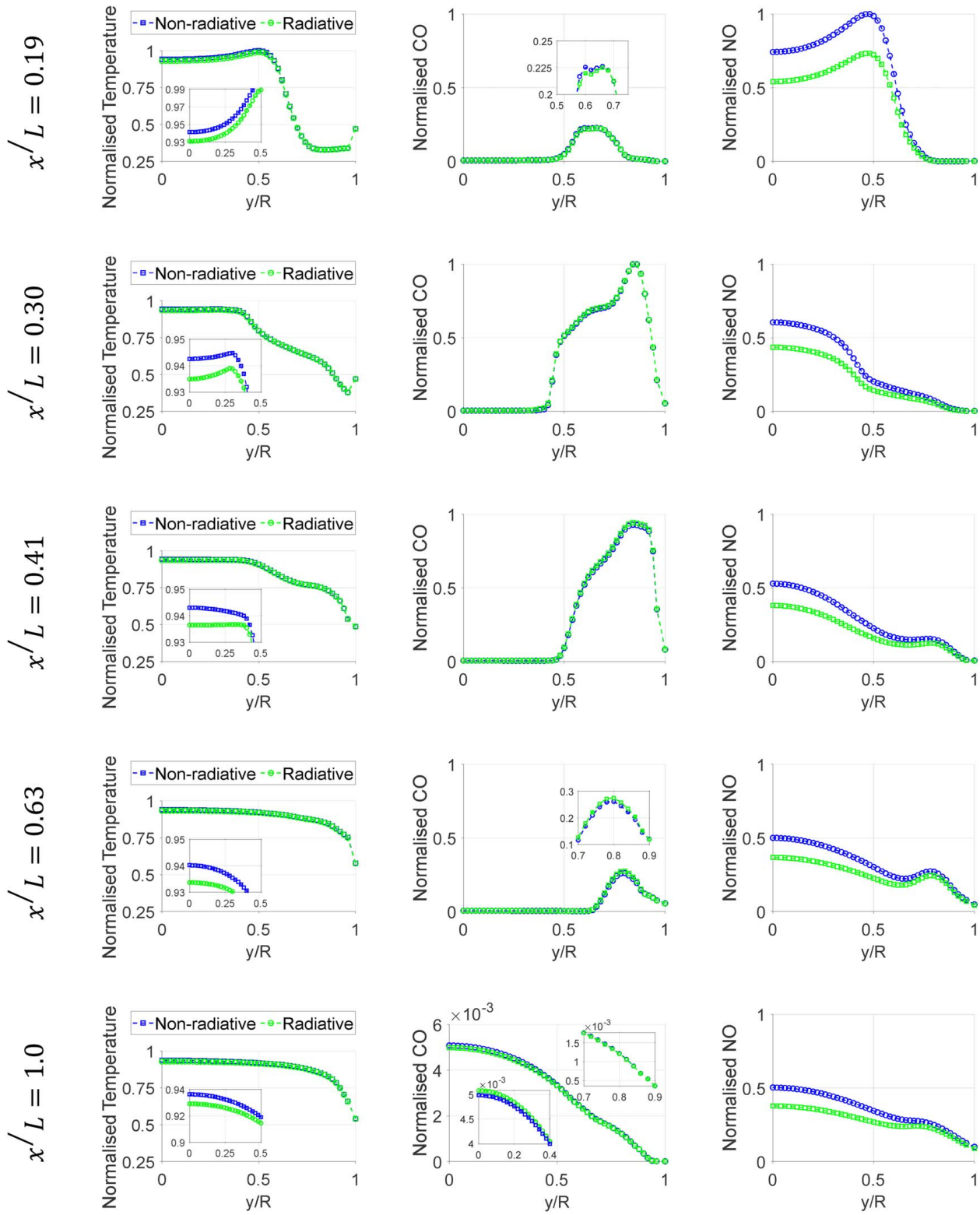


Fig. 9 Radial averaged temperature, CO and NO at normalized axial positions for radiative and non-radiative cases

cone-shaped outlet shown in Fig. 1. Towards the combustor outlet, $x/L = 1$, the radial temperature profile is observed to be more radially uniform, with lower values closer to the liner wall. These plots also show that the differences in temperatures between the radiative and non-radiates cases begin to narrow with distance from the heat source.

The radial profiles for CO and NO show the different scale of influence of the radiation effects. The CO concentration around the combustor center is almost consistently flat throughout the combustor, axially up to $x/L = 0.63$. This area coincides with the high-temperature region that helps to mitigate CO. This is not the case at the exit of the combustor ($x/L = 1$) at the radial position from 0 to 0.5, resulting from the slowdown of the burnout from the pilot diffusion flame burner. Also in this axial position, between 0.5 and 1, there is a suppression in CO compared to preceding locations. This is due to fewer CO leftover

Downloaded from http://asmedigitalcollection.asme.org/openengineering/article-pdf/doi/10.1115/1.4055983/6942616/aoje_1_011051.pdf by guest on 22 November 2022

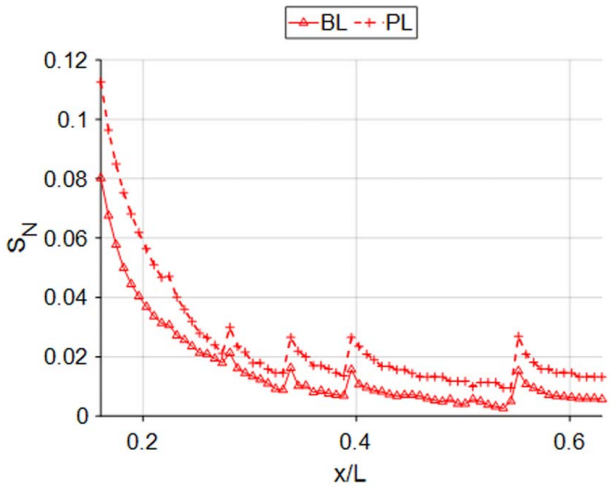


Fig. 10 Normalized unmixedness across the combustor—baseload and part-load

because of a more distributed temperature profile towards the liner wall. The increase in the temperature near the liner wall then induces CO burnout. The NO concentration profiles show the most significant difference between the non-radiative and radiative cases at a normalized axial distance of 0.19. The differences between the two generally reduce further away from the burner outlet. The profiles towards the outlet of the combustor become more radially uniform around $y/R > 0.5$, resulting from a growing contribution of NO from the main burner. This is consistent with the higher temperatures around the wall at the exit of the combustor.

5 Effect of Fuel–Air Unmixedness on Performance and Emissions

The study of fuel–air unmixedness compares the non-reacting and reaction simulations. Radiation has been included in the baseload and part-load (distinguished by different combustor inlet pressures and temperatures) cases to account for the heat losses. The objective here is to show the characteristics of each operating condition, also their influence on combustion performance and emissions from the perspective of the unmixedness. The information on the unmixedness for both operating conditions is extracted from the respective non-reaction simulations. Figure 10 shows the unmixedness across the combustor at baseload and part-load. The unmixedness was derived from the results of the non-reacting case, while the temperature and reaction progress were obtained from the reacting case. The area of interest has been limited between the burner outlet and the bypass valve. The figure shows that for both load conditions, the unmixedness decays with distance across the combustor. The rapid reduction upstream (between $x/L = 0.16$ and 0.35) can be attributed to the recirculation zone that accelerates the mixing close to the burner outlet. As mentioned previously, this is facilitated by the pilot burner cone. Discontinuities are observed in the profiles because of the incoming cooling flow at the combustor midsection and transition piece. The mixing within the combustor is considered reasonable, despite not reaching an absolute 0, where fuel and air are perfectly mixed. The influence of the cooling flows is such that it introduces additional unmixed air into the mixing process, changing the effective equivalence ratio and, in turn, increasing the unmixedness around those areas.

Table 3 Normalized unmixedness at the burner exit

	Normalized unmixedness, S_N	
Operating conditions	Main burner exit	Pilot burner exit
Baseload	0.0830	0.0088
Part-load	0.1154	0.0381

Table 3 shows the plane average values of unmixedness at the exit of the main and pilot burners for the baseload and part-load. The unmixedness at the pilot burner exit is lower than the main burner in both operating conditions, signifying better mixing quality at the former. With more swirler vanes and a higher swirler vane outlet angle than in the main burner, the mixing achieved in the pilot burner is intended to form zones of equivalence ratio favorable to combustion within the reaction zone. Hence, it can be expected that the combustion initiates from the pilot burner. Between the two operating conditions, the unmixedness at the baseload is lower than at the part-load. This explains the higher burner exit temperature in the part-load than in the baseload. The poor unmixedness at part-load is designed to maintain combustion stability at this load, resulting in the flame temperature being as high as the baseload. Hence, the bypass valve is in operation to help reduce the flame temperature to a value that matches the respecting load. The table shows that the main burner has a higher unmixedness that becomes worse at part-load compared to baseload.

Figure 11 shows the unmixedness and turbulence kinetic energy (TKE), k, profiles along with the streamlines depicting the recirculation zone of both operating conditions. The TKE is extracted from the reacting flow simulation. The rapid decrease in unmixedness from its highest values set by the main burner of each operating condition can be observed before the recirculation center. This brings about a high turbulence production that is in favor of the mixing

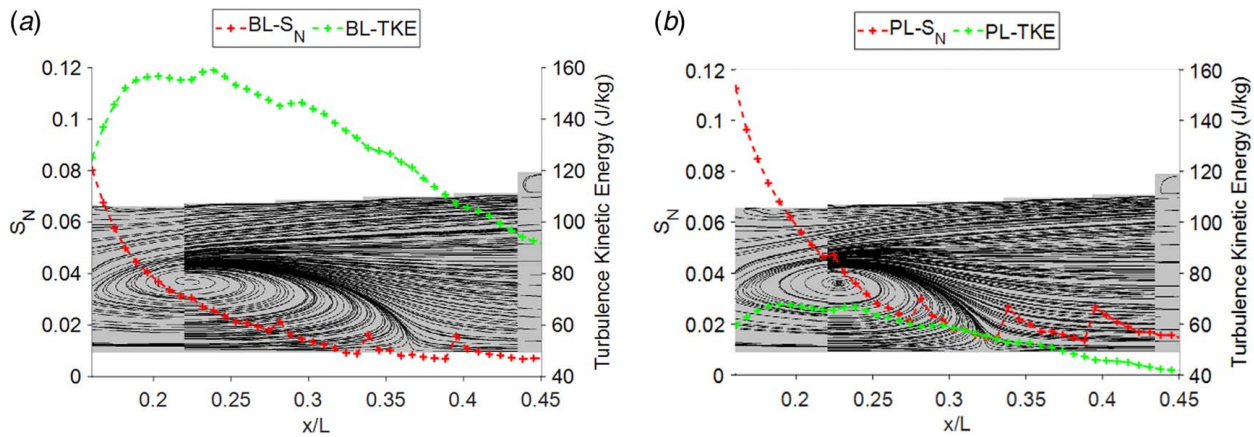


Fig. 11 Recirculation zone profiles of normalized unmixedness and mass-averaged TKE: (*a*) baseload and (*b*) part-load

Downloaded from http://asmedigitalcollection.asme.org/openengineering/article-pdf/doi/10.1115/1.4055983/6942616/aoje_1_011051.pdf by guest on 22 November 2022

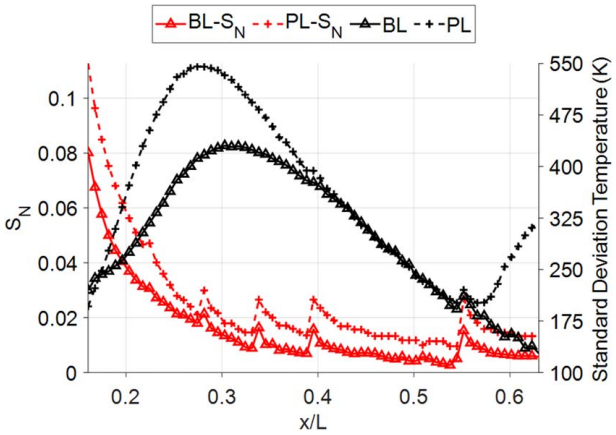


Fig. 12 Unmixedness and standard deviation temperature at baseload and part-load

process, as seen from the figure. As the influence of the recirculation reduces downstream, the unmixedness sees little change while the TKE continues to decay. The mixture at this point is likely to be dominated by the unburnt premixed mixture from the main burner. The unmixedness is becoming more favorable for combustion due to the interaction with the flow of mixtures from other burners and the recirculation zone. This is similar to the one at the upstream position. Hence, from this point onwards, the rise in the temperature and the reaction progress is further contributed by the burning of the main premixed mixture as it starts to combust with the heat release produced from the pilot flame. Figure 12 shows the unmixedness profile alongside the temperature mass-weighted standard deviation profile. This shows how the unmixedness relates to temperature standard deviation. Both operating conditions experience a gradual increase in the temperature standard deviation marking the start of the combustion; in this case, the air/fuel mixture ignition is initiated at the pilot burner. The baseload, having lower unmixedness, peaks at a level of temperature variation below the part-load. The relatively higher unmixedness in the part-load leads to a relatively higher range of temperature variation and thus higher NO emissions. Reaction progress at part-load is also higher, indicating a high conversion rate from the unburnt to burnt mixtures. The baseload's temperature variation continues to decrease downstream. The increase in the part-load temperature variation profile for $x/L > 0.55$ is due to the influence of the air from the bypass valve and is not related to the combustion process. The rate of increase in the temperature and reaction progress in the part-load is also slower than the

Table 4 Pathway contribution to the formation of total NO at the combustor outlet

Operating conditions	Thermal NO	Prompt NO	N_2O pathway
Baseload	72.45%	0.03%	27.53%
Part-load	97.16%	0.01%	2.83%

baseload. From Fig. 11, it is also clear that the part-load recirculation zone is relatively short in terms of axial length than the baseload, which then confirms the lag. Despite that, the baseload is indeed expected to operate in this way, as it has a purpose to lower the consequence of having excessive emissions levels.

5.1 Emissions Analysis. Through the temperature variation, the emission analysis of each operating condition can be examined.

Figure 13 shows the emissions profiles (of baseload and part-load) and the standard deviation temperature. The values of the concentrations have been normalized using the value of the maximum concentration in each plot. For this part of the study, the area of interest was extended up until the combustor outlet where $x/L = 1$. As indicated previously, the part-load has a second peak standard temperature deviation that is reduced by the bypass air used in this operation. This location corresponds to the dip in NO at $x/L = 0.65$.

The rapid increase of the CO formation is observed to be up to $x/L < 0.3$, where the temperature standard deviation is also rising to peak values. Likewise, the subsequent drop in deviation temperature relates to a decrease in CO. At the early stage of the combustion, the CO concentration is relatively lower in the baseload than the part-load, albeit with a similar CO formation rate. However, the peak value of the CO at the baseload is greater; the final CO levels attained are lower compared to the part-load. This is because of a generally smaller deviation of the temperature in relation to the part-load. Also as shown on the right of the figure, the baseload has greater mass-averaged temperature towards the combustor outlet that facilitates better CO burnout. The peak value of the NO concentration is about 2.7 times the peak CO concentration. NO values at part-load are much greater than the baseload across the combustor but only so in parts, for normalized mass-averaged temperatures. A small reduction in the NO values is observed at $x/L = 0.6$, due to bypass air introduced into the transition piece. This slightly reduces the mass-averaged temperature for the part-load case beyond $x/L = 0.6$. The NO trends generally follow the normalized mass-average temperatures. Despite using the bypass air for cooling (not implemented at baseload), the NO values at the exit

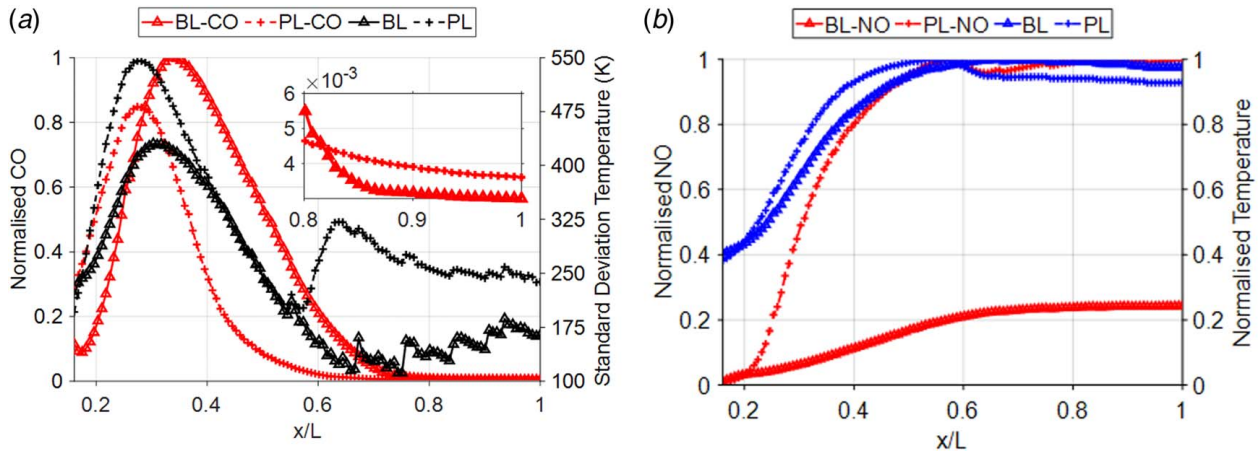


Fig. 13 Pollutants, their standard deviation temperature, and normalized mass-average temperature for baseload and part-load: (*a*) CO concentration and (*b*) NO concentration

Downloaded from http://asmedigitalcollection.asme.org/openengineering/article-pdf/doi/10.1115/1.4055983/6942616/aoje_1_011051.pdf by guest on 22 November 2022

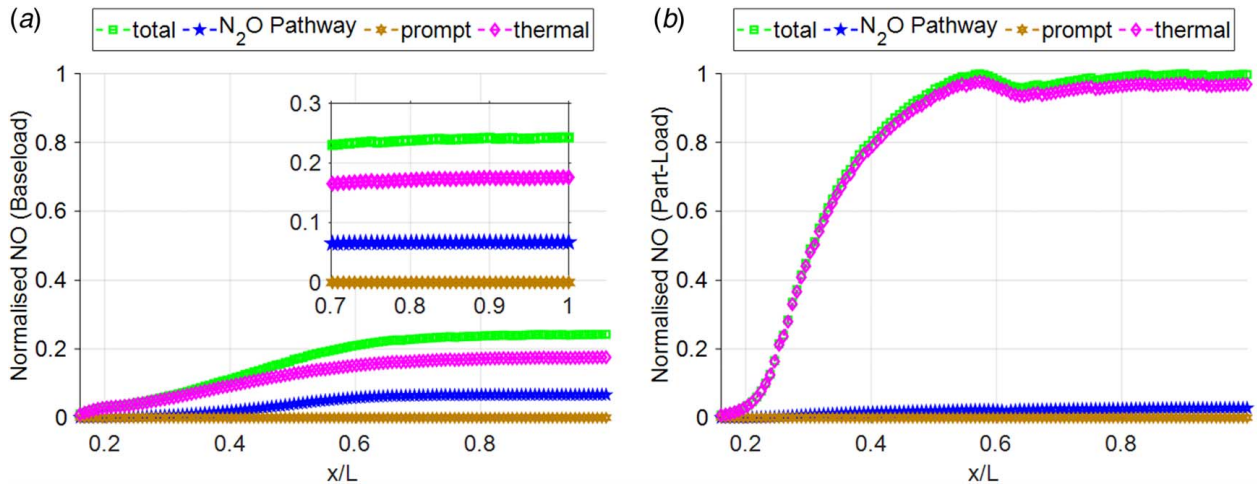


Fig. 14 Contribution of different formation pathways to the total NO: (*a*) baseload (*b*) part-load

of the combustor remain greater at part-load. This is because of its significantly higher pilot equivalence ratio as shown in Table 1 and relatively poorer unmixedness as shown in Table 3. For both operations, the NO continues to increase towards the combustor outlet. The increasing trend is likely due to increasing the combustor residence time.

The percentage contributing pathways to total NO for both operating conditions at the exit of the combustor are presented in Table 4. Additionally, Fig. 14 shows the contribution of each pathway at baseload and part-load. Each pathway has been normalized with the maximum value of NO from the part-load. The prompt NO is consistently low in both operating conditions. The formation of prompt NO depends on the availability of small hydrocarbon radicals within the thin flame sheet close to the burners. The hydrocarbon radicals reduce in concentration moving downstream from the burner, hence low prompt NO. In this work, the increase in the prompt NO is far less than the other pathways. Despite being in the pilot fuel-rich environment during part-load, the temperature is not low enough for the prompt NO to form in a significant amount. With a temperature over 1800 K,

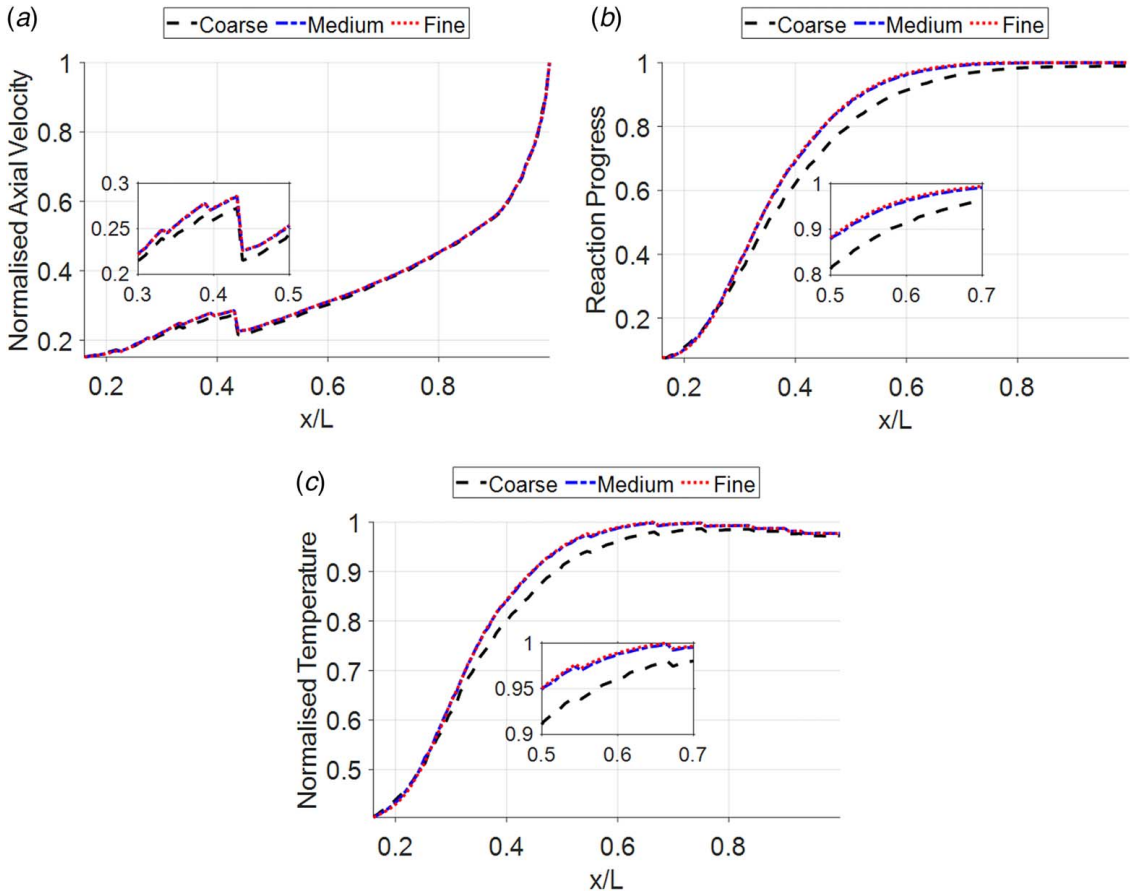


Fig. 15 From left-to-right: (*a*) mass-averaged velocity axial, (*b*) mass-averaged reaction progress, and (c) mass-averaged temperature

Downloaded from http://asmedigitalcollection.asme.org/openengineering/article-pdf/doi/10.1115/1.4055983/6942616/aoje_1_011051.pdf by guest on 22 November 2022

the figure shows thermal NO as the most dominant from the burner outlet to the combustor outlet. Hence the shape of the profile is consistent with the total NO. N_2O contribution is also shown to be consistently low, though greater than prompt NO, resulting from the high temperatures.

6 Conclusions

Numerical investigations have been carried out on a DLN combustor to justify accounting for radiation heat losses in modeling, also showing the influence of fuel–air unmixedness (mixing quality). This has been substantiated with respect to the combustor performance and emissions, and the differences that it makes. The study has shown:

- That accounting for radiation effect in the modeling reduces the combustor outlet temperature by 0.41%. This subsequently reduces the NO by 17.6% with a negligible decrease in CO.
- In the total NO reduction, thermal and prompt formation pathways are the contributors to the decrease, as opposed to N_2O that increased.
- From the radial profiles of temperatures and emissions of non-radiative and radiative cases, NO prediction shows the highest disparity closer to the burner outlet/pilot flame. The differences reduce axially towards the combustor exit. Nevertheless, the reduced flame temperature in the radiation case (caused by heat losses between the combustion flame and its surroundings) justifies the comparatively lower NO.
- Unmixedness generally improves (reduces) across the combustor from upstream to downstream. This is due to the interactions of the mixture with the rest of the flow from the burners. However, small increases can be incited by cooling flows.
- That the pilot burner has the lower unmixedness, indicating superior mixing than the main burners. This is attributed to more swirler vanes and higher swirler vane outlet angles in the pilot burner.
- The TKE in the reacting flow shows a direct relationship with the unmixedness in the non-reacting flow. The TKE value peaks around the recirculation zone where the unmixedness significantly drops.
- The comparison between the temperature standard deviation and the unmixedness shows poorer unmixedness during part-load that contributes to the high-temperature variation at the early stage of the combustion. This is shown to be beneficial in maintaining lower CO concentration than the baseload, only at the early stage of combustion. At the outlet of the combustor, the part-load CO and NO are above the emissions in the baseload. Also, the thermal NO contribution to the total NO is 25% point higher at part-load.

Acknowledgment

This study was part of the TURBO-REFLEX project that has received funding from the European Union's Horizon 2020 research and innovation program, under grant agreement no. 764545.

Conflict of Interest

There are no conflicts of interest. This article does not include research in which human participants were involved. Informed consent not applicable. This article does not include any research in which animal participants were involved.

Data Availability Statement

The authors confirm that most of the data and methodology supporting the findings of this study are available within the article. Further data are not publicly available due to commercial and intellectual property rights.

Nomenclature

c = reaction progress
f = mixture fraction
k = turbulence kinetic energy
l = length scale
n = refractive index of the medium
p = pressure
q = heat flux
t = time
u = velocity vector
v = fluctuation variable
x = spatial direction
A = total surface area of fluid boundaries
C = fuel mass fraction
D = molecular diffusivity
G = incident radiation
H = enthalpy
L = combustor model length
S = modulus of mean rate-of-strain tensor
T = temperature
U = flame speed
V = diffusive velocity
W = mass flowrate
Y = mass fraction of species
q_r = radiative heat flux
C_p = heat capacity at constant pressure
$I_{b\eta}$ = Planck function or blackbody intensity
M_w = molecular weight
S_f = fuel distribution mass-weighted average standard deviation or unmixedness
S_N = normalized unmixedness
S_{FAR} = coefficient of mass-based FAR
$P(v)$ = PDF of variable v
Sc = Schmidt number

Greek Symbols

a_ε = emissivity weighting factor
ε = turbulence dissipation rate
ε^* = modified turbulence dissipation rate
ε = emissivity
κ = absorption coefficient
μ = viscosity
ρ = density
ϱ = sum of partial pressures of all absorbing gases
σ = Stefan–Boltzmann constant
τ = viscous stress tensor
ν = volume of fluid
ϕ = equivalence ratio
ω = reaction source term
∇ = gradient

Subscripts

$_{i,\,j}$ = direction vector indexes
$_k$ = kth species index
$_l$ = laminar flow properties
$_n$ = nth cell number
$_{NO}$ = NO (nitric oxide) species
$_t$ = turbulent flow properties
$_u$ = unburnt mixture
$_w$ = radiation properties on the wall
$_{\eta,\ldots,\eta}$ = spectral-related radiation properties

Downloaded from http://asmedigitalcollection.asme.org/openengineering/article-pdf/doi/10.1115/1.4055983/6942616/aoje_1_011051.pdf by guest on 22 November 2022

Letters and Symbols

$\widetilde{c'^2}$ = reaction progress variance
$\widetilde{f'^2}$ = mixture fraction variance

Headings

$\tilde{}$ = mean part from scalar decomposition/density-weighted averaged
$\hat{}$ = fluctuating part from scalar decomposition
$\bar{}$ = non-weighted averaged
$\vec{}$ = vector

Appendix AReferences

[1] Fric, T. F., 1993, "Effects of Fuel-Air Unmixedness on NO(x) Emissions," J. Propuls. Power, **9**(5), pp. 708–713.
[2] Barnes, J. C., Mello, J. P., Mellor, A. M., and Malte, P. C., 1996, "Preliminary Study of NOx, CO, and Lean Blowoff in a Piloted-Lean Premixed Combustor. Part 1: Experimental," The Combustion Institute, Pittsburgh, PA.
[3] Stufflebeam, J. H., Kendrick, D. W., Sowa, W. A., and Snyder, T. S., 2002, "Quantifying Fuel/Air Unmixedness in Premixing Nozzles Using an Acetone Fluorescence Technique," ASME J. Eng. Gas Turbines Power, **124**(1), pp. 39–45.
[4] Seo, S., and Lee, S.-Y., 2010, "Effects of Unmixedness on Combustion Instabilities in a Lean-Premixed Gas Turbine Combustor," Flow Turbul. Combust., **85**(1), pp. 95–112.
[5] Li, S., Zhang, S., Hou, L., and Ren, Z., 2018, "Analysis of the Mixing and Emission Characteristics in a Model Combustor," Volume 4B: Combustion, Fuels, and Emissions, Oslo, Norway, June 11–15, pp. 1–7.
[6] Lefebvre, A. H., 1984, "Flame Radiation in Gas Turbine Combustion Chambers," Int. J. Heat Mass Transfer, **27**(9), pp. 1493–1510.
[7] Viskanta, R., 1987, "Radiation Heat Transfer in Combustion Systems," Prog. Energy Combust. Sci., **13**(2), pp. 97–160.
[8] Park, S., Kim, J. A., Ryu, C., Chae, T., Yang, W., Kim, Y. J., Park, H. Y., and Lim, H. C., 2013, "Combustion and Heat Transfer Characteristics of oxy-Coal Combustion in a 100MWe Front-Wall-Fired Furnace," Fuel, **106**, pp. 718–729.
[9] Wang, J., Xue, Y., Zhang, X., and Shu, X., 2015, "Numerical Study of Radiation Effect on the Municipal Solid Waste Combustion Characteristics Inside an Incinerator," Waste Manage., **44**, pp. 116–124.
[10] Ji, J., Sivathanu, Y. R., and Gore, J. P., 2000, "Thermal Radiation Properties of Turbulent Lean Premixed Methane Air Flames," Proc. Combust. Inst., **28**(1), pp. 391–398.
[11] Thellmann, A., and Mundt, C., 2009, *Modelling of Radiation Heat Transfer in Reacting Hot Gas Flows*, European Space Agency (Special Publication), Noordwijk, Netherlands.
[12] Edge, P., Porter, R., Pourkashanian, M., and Williams, A., 2009, "A Quantitative Study of the Performance of Commercial Radiation Models for Predicting Behaviour of oxy-Coal Combustion," IEA GHG 1st Oxyfuel Conference, Cottbus, Germany, Sept. 8–11, pp. 1–21.
[13] Ebrahimi Fordoei, E., and Mazaheri, K., 2019, "Numerical Study of Chemical Kinetics and Radiation Heat Transfer Characteristics on the Temperature Distribution in the oxy-Fuel Combustion," Heat Mass Transfer, **55**(7), pp. 2025–2036.
[14] Khodabandeh, E., Moghadasi, H., Pour, M. S., Ersson, M., Jönsson, P. G., Rosen, M. A., and Rahbari, A., 2020, "CFD Study of Non-Premixed Swirling Burners: Effect of Turbulence Models," Chin. J. Chem. Eng., **28**(4), pp. 1029–1038.
[15] Pang, Y. S., Law, W. P., Pung, K. Q., and Gimbun, J., 2018, "A Computational Fluid Dynamics Study of Turbulence, Radiation, and Combustion Models for Natural Gas Combustion Burner," Bull. Chem. React. Eng. Catal., **13**(1), p. 155.
[16] Danckwerts, P. V., 1952, "The Definition and Measurement of Some Characteristics of Mixtures," Appl. Sci. Res., **3**(4), pp. 279–296.
[17] Dimotakis, P. E., and Miller, P. L., 1990, "Some Consequences of the Boundedness of Scalar Fluctuations," Phys. Fluids A Fluid Dyn., **2**(11), pp. 1919–1920.
[18] Hornsby, C., and Norster, E. R., 1997, "Application of CFD to DLN Combustion," Volume 2: Coal, Biomass and Alternative Fuels; Combustion and Fuels; Oil and Gas Applications; Cycle Innovations, Orlando, FL, June 2–5, pp. 1–8.
[19] Biagioli, F., and Güthe, F., 2007, "Effect of Pressure and Fuel–Air Unmixedness on NOx Emissions From Industrial Gas Turbine Burners," Combust. Flame, **151**(1–2), pp. 274–288.
[20] Iba, H., Nomura, M., Kawakami, T., and Koga, T., 2003, "Advanced Monitoring System for Combustor Pressure Fluctuation," Proceedings of the International Gas Turbine Congress 2003, Tokyo, Japan, Nov. 2–7, pp. 1–4.
[21] Tanimura, S., Nose, M., Ishizaka, K., Takiguchi, S., and Rodriguez, J., 2008, "Advanced Dry Low NOx Combustor for Mitsubishi G Class Gas Turbines," Volume 3: Combustion, Fuels and Emissions, Parts A and B, Berlin, Germany, June 9–13, pp. 607–615.
[22] Ruan, S., Swaminathan, N., Isono, M., Saitoh, T., and Saitoh, K., 2015, "Simulation of Premixed Combustion With Varying Equivalence Ratio in Gas Turbine Combustor," J. Propuls. Power, **31**(3), pp. 861–871.
[23] Emami, M. D., Shahbazian, H., and Sunden, B., 2019, "Effect of Operational Parameters on Combustion and Emissions in an Industrial Gas Turbine Combustor," ASME J. Energy Resour. Technol., **141**(1), p. 012202.
[24] Jeong, D., and Huh, K. Y., 2009, "Numerical Simulation of Non-Reacting and Reacting Flows in a 5MW Commercial Gas Turbine Combustor," Volume 2: Combustion, Fuels and Emissions, Orlando, FL, June 8–12, pp. 739–748.
[25] Cardoso de Souza, T., Bastiaans, R. J. M., Geurts, B. J., and De Goey, L. P. H., 2011, "LES and RANS of Premixed Combustion in a Gas-Turbine Like Combustor Using the Flamelet Generated Manifold Approach," Volume 2: Combustion, Fuels and Emissions, Parts A and B, Vancouver, British Columbia, Canada, June 6–10, pp. 1119–1127.
[26] Park, J. S., Yun, N., Moon, H., Kim, K. M., Kang, S. H., and Cho, H. H., 2011, "Thermal Analysis of Cooling System in a Gas Turbine Transition Piece," Proceedings of the ASME Turbo Expo, Vancouver, British Columbia, Canada, June 6–10, Vol. 5, pp. 1915–1924.
[27] Mansouri, Z., and Boushaki, T., 2018, "Experimental and Numerical Investigation of Turbulent Isothermal and Reacting Flows in a Non-Premixed Swirl Burner," Int. J. Heat Fluid Flow, **72**, pp. 200–213.
[28] Pampaloni, D., Nassini, P. C., Andreini, A., Facchini, B., and Cerutti, M., 2020, "Numerical Investigations of Pollutant Emissions From Novel Heavy-Duty Gas Turbine Burners Operated With Natural Gas," ASME J. Eng. Gas Turbines Power, **142**(3), p. 031025.
[29] Peters, N., 1988, "Laminar Flamelet Concepts in Turbulent Combustion," Symp. Combust., **21**(1), pp. 1231–1250.
[30] Zhang, K., Ghobadian, A., and Nouri, J. M., 2017, "Comparative Study of Non-premixed and Partially-Premixed Combustion Simulations in a Realistic Tay Model Combustor," Appl. Therm. Eng., **110**, pp. 910–920.
[31] Zimont, V., Polifke, W., Bettelini, M., and Weisenstein, W., 1998, "An Efficient Computational Model for Premixed Turbulent Combustion at High Reynolds Numbers Based on a Turbulent Flame Speed Closure," ASME J. Eng. Gas Turbines Power, **120**(3), pp. 526–532.
[32] Ihme, M., and Pitsch, H., 2008, "Modeling of Radiation and Nitric Oxide Formation in Turbulent Nonpremixed Flames Using a Flamelet/Progress Variable Formulation," Phys. Fluids, **20**(5), p. 055110.
[33] Pampaloni, D., Nassini, P. C., Paccati, S., Palanti, L., Andreini, A., Facchini, B., Cerutti, M., and Riccio, G., 2018, "Numerical Predictions of Pollutant Emissions of Novel Natural Gas Low NOx Burners for Heavy Duty Gas Turbine," 2018 Joint Propulsion Conference, Cincinnati, OH, July 9–11, pp. 1–12.
[34] De Soete, G. G., 1975, "Overall Reaction Rates of NO and N2 Formation From Fuel Nitrogen," Symp. Combust., **15**(1), pp. 1093–1102.
[35] Malte, P. C., and Pratt, D. T., 1975, "Measurement of Atomic Oxygen and Nitrogen Oxides in Jet-Stirred Combustion," Symp. Combust., **15**(1), pp. 1061–1070.
[36] Goebel, F., Kniesner, B., Frey, M., Knab, O., and Mundt, C., 2014, "Radiative Heat Transfer Analysis in Modern Rocket Combustion Chambers," CEAS Space J., **6**(2), pp. 79–98.
[37] Modest, M. F., and Haworth, D. C., 2016, "Radiation Properties, RTE Solvers, and TRI Models," *Radiative Heat Transfer in Turbulent Combustion Systems: Theory and Applications*, F. A. Kulacki, ed., Springer International Publishing, Cham, pp. 43–83.
[38] Modest, M. F., 2013, "The Method of Spherical Harmonics (P-Approximation)," *Radiative Heat Transfer*, 3rd ed., M. F. Modest, ed., Elsevier, Boston, MA, pp. 495–540.
[39] Goebel, F., and Mundt, C., 2011, "Implementation of the P1 Radiation Model in the CFD Solver NSMB and Investigation of Radiative Heat Transfer in the SSME Main Combustion Chamber," 17th AIAA International Space Planes and Hypersonic Systems and Technologies Conference, San Francisco, CA, Apr. 11–14, pp. 1–11.
[40] Özışık, M. N., 1973, *Radiative Transfer and Interactions With Conduction and Convection*, Wiley, New York.
[41] Hottel, H. C., and Sarofim, A. F., 1967, *Radiative Transfer*, McGraw-Hill, New York.
[42] Modest, M. F., 1991, "The Weighted-Sum-of-Gray-Gases Model for Arbitrary Solution Methods in Radiative Transfer," ASME J. Heat Transfer-Trans. ASME, **113**(3), pp. 650–656.
[43] Sun, X., Agarwal, P., Carbonara, F., Abbott, D., Gauthier, P., and Sethi, B., 2020, "Numerical Investigation Into the Impact of Injector Geometrical Design Parameters on Hydrogen Micromix Combustion Characteristics," Volume 3: Ceramics; Coal, Biomass, Hydrogen, and Alternative Fuels, Virtual Online, Sept. 21–25, pp. 1–11.
[44] Akamatsu, S. and Dowling, A. P., 2001, "Three Dimensional Thermoacoustic Oscillation in a Premix Combustor," Volume 2: Coal, Biomass and Alternative Fuels; Combustion and Fuels; Oil and Gas Applications; Cycle Innovations, New Orleans, LA, June 4–7, Vol. 2, pp. 1–12.
[45] Hada, S., Nakamura, S., Tanaka, K., Akagi, K., Konishi, T., and Shibata, H., 2014, "Transition Piece of Combustor, Gas Turbine Having the Same, and Producing Method for Transition Piece," US 8769957 B2, Mitsubishi Heavy Industries, Ltd. Tokyo.
[46] Lefebvre, A. H., and Ballal, D. R., 2010, *Gas Turbine Combustion*, 3rd ed., CRC Press, Boca Raton, FL.
[47] Tanaka, K., Nishida, K., and Akizuki, W., 2009, "Gas Turbine Combustor Technology Contributing to Environmental Conservation," Mitsubishi Heavy Ind. Tech. Rev., **46**(2), pp. 6–12.
[48] Abudu, K., Igie, U., Minervino, O., and Hamilton, R., 2020, "Gas Turbine Minimum Environmental Load Extension With Compressed Air Extraction for Storage," Appl. Therm. Eng., **180**, p. 115869.

Downloaded from http://asmedigitalcollection.asme.org/openengineering/article-pdf/doi/10.1115/1.4055983/6942616/aoje_1_011051.pdf by guest on 22 November 2022



https://dspace.org/

Numerical study of radiation and fuel-air unmixedness on the performance of a dry low NOx combustor

Wiranegara, Raditya Yudha; Igie, Uyioghosa; Ghali, Pierre; Zhao, Rang; Abbott, David ...

2022-11-11
American Society of Mechanical Engineers (ASME)
https://doi.org/10.1115/1.4055983
Wiranegara RY, Igie U, Ghali P, et al., (2022) Numerical study of radiation and fuel-air unmixedness on the performance of a dry low NOx combustor, ASME Open Journal of Engineering, Volume 1, January, 2022, Article number 011051

Downloaded from a DSpace repository. https://dspace.org/